



Low tungsten content of nanostructured material supported on carbon for the degradation of phenol

M.H.M.T. Assumpção^a, R.F.B. De Souza^a, R.M. Reis^b, R.S. Rocha^b, J.R. Steter^b, P. Hammer^c, I. Gaubeur^a, M.L. Calegaro^b, M.R.V. Lanza^b, M.C. Santos^{a,*}

^a LEMN – Laboratório de Eletroquímica e Materiais Nanoestruturados – CCNH – Centro de Ciências Naturais e Humanas, UFABC – Universidade Federal do ABC, CEP 09.210-170, Rua Santa Adélia 166, Bairro Bangú, Santo André, SP, Brazil

^b Instituto de Química de São Carlos, USP – Universidade de São Paulo, Caixa Postal 780, CEP 13.560-970, São Carlos, SP, Brazil

^c Instituto de Química, UNESP – Universidade Estadual Paulista, 14801-970 Araraquara, SP, Brazil



ARTICLE INFO

Article history:

Received 4 October 2012

Received in revised form 3 May 2013

Accepted 10 May 2013

Available online 21 May 2013

Keywords:

Hydrogen peroxide electrogeneration

Tungsten oxide

Phenol degradation

ABSTRACT

A comparative study using different mass proportions of WO_3/C (1%, 5%, 10% and 15%) for H_2O_2 electro-generation and subsequent phenol degradation was performed. To include the influence of the carbon substrate and the preparation methods, all synthesis parameters were evaluated. The WO_3/C materials were prepared by a modified polymeric precursor method (PPM) and the sol-gel method (SGM) on Vulcan XC 72R and Printex L6 carbon supports, verifying the most efficient metal/carbon proportion. The materials were physically characterized by X-ray diffraction (XRD) and by X-ray photoelectron spectroscopy (XPS) techniques. The XRD and the XPS techniques identified just one phase containing WO_3 and elevated oxygen concentration on carbon with the presence of WO_3 . The oxygen reduction reaction (ORR), studied by the rotating ring-disk electrode technique, showed that WO_3/C material with the lowest tungsten content (1% WO_3/C), supported on Vulcan XC 72R and prepared by SGM, was the most promising electrocatalyst for H_2O_2 electro-generation. This material was then analyzed using a gas diffusion electrode (GDE) and 585 mg L⁻¹ of H_2O_2 was produced in acid media. This GDE was employed as a working electrode in an electrochemical cell to promote phenol degradation by an advanced oxidative process. The most efficient method applied was the photo-electro-Fenton; this method allowed for 65% degradation and 11% mineralization of phenol during a 2-h period. Following 12 h of exhaustive electrolysis using the photo-electro-Fenton method, the total degradation of phenol was observed after 4 h and the mineralization of phenol approached 75% after 12 h.

© 2013 Elsevier B.V. All rights reserved.

1. Introduction

Sewage discharge without sufficient treatment is the main source of organic impurities in surface water [1]. Water contamination by sewage presents great difficulties for conventional water treatment and many additional processes, including coagulation/filtration, softening, membrane processing, ion exchange and granular activated carbon filtration also produce residuals. Therefore, as discharge quality requirements become more stringent, treatment of waste residuals must improve accordingly [1,2].

Aromatic compounds are common pollutants in the waste effluent discharged by many factories and industry processes, including chemical plants, petroleum refineries, phenolic resins, caprolactam textile facilities and some pharmaceutical processes [3,4]. Among the aromatic compounds, the phenolic products are toxic

to humans and aquatic organisms and are listed as one of the most common and serious environmental contaminants in water [4]. Due to the toxicity and consequent health hazards of phenolic compounds, these products have been placed on the list of priority pollutants by the U.S. Environmental Protection Agency [5].

Among the existing processes for water treatment are the advanced oxidation processes (AOPs), which are considered to be promising, as “environmentally friendly” processes. Environmentally friendly processes boast a high degradation capacity [6–8], complete mineralization [9,10] or oxidation to very low concentrations [11,12] and the production of environmentally friendly byproducts [7,13,14]. AOPs can be defined as aqueous phase oxidation methods that involve *in situ* generation of highly reactive species such as hydroxyl radicals, which are the most powerful oxidizing species after fluorine (possessing an oxidation potential of 2.80 V) [7,15]. These reactive species lead to the destruction of the pollutant [15].

Hydroxyl radicals for water and wastewater treatment can be generated by several process including the following: H_2O_2/UV ,

* Corresponding author. Tel.: +55 11 4996 0163; fax: +55 11 4996 0090.

E-mail addresses: mauro.santos@ufabc.edu.br, drmcas@gmail.com (M.C. Santos).

O_3 /UV, Fenton's reagent, O_3/H_2O_2 /UV, TiO_2 [7,8,16] and more recently, the homogeneous H_2O_2 /UV and photo-Fenton process. The H_2O_2 /UV and photo-Fenton process has been used in the treatment of organic pollutants, exhibiting important advantages over processes based on the irradiation of suspended solid photocatalysts [8].

Hydrogen peroxide, used to generate the hydroxyl radical and H_2O_2 , is considered to be a green chemical when utilized as replacement for chlorine in the treatment of wastewater. Additionally, H_2O_2 can be generated via two-electron transfer in the oxygen reduction reaction, and carbon electrodes are the reference material for H_2O_2 production in alkaline media [17–19]. The use of some metal oxides to enhance the activity of the oxygen reduction reaction to promote the two-electron transfer has already been described [20–22].

The production of electrocatalysts composed of metal oxides and supported on carbon has recently utilized nanostructured transition metal oxide semiconductors because of their large surface area and unique physical properties [23]. Among the various oxides, tungsten trioxide (WO_3) is of scientific and technological interest because its optical and electronic properties make it a promising material for use in photocatalysis, electrochromic and sensing device applications [24]. WO_3 is an n-type semiconductor and it has relatively high electrical conductivity, such that it may be one of the most promising materials for wastewater treatment [25,26].

To improve the hydrogen peroxide electrogeneration, this work describes a comparative study of four compositions of tungsten oxide nanoparticles supported on carbon (1%, 5%, 10% and 15% WO_3/C) as electrocatalysts for ORR. Considering that the preparation methodology [21] and the carbon supports [6] could also influence hydrogen peroxide production, this work also evaluated the effects of the preparation method and the carbon support. Additionally, we identified the best electrocatalyst for H_2O_2 electrogeneration using a gas diffusion electrode (GDE). Finally, phenol degradation was studied using several AOPs, and a reaction mechanism for its degradation process was proposed.

2. Materials and methods

2.1. WO_3 preparation

Various concentrations (1%, 5%, 10% and 15%, w/w) of tungsten trioxide electrocatalysts were first prepared using the polymeric precursor method (PPM), as described in our previous studies [21,22]. Tungsten chloride (Aldrich) and Vulcan XC 72 R (Cabot Corporation) were used in order to find the best composition for H_2O_2 electrogeneration. Once we determined the best proportion of tungsten using the Vulcan XC 72R carbon as a support and the PPM, the best tungsten proportion was then prepared using the sol–gel method (SGM) as previously described [21,27] and the Printex L6 (Evonik) was used as the carbon support. These tungsten materials were used to evaluate the effects of preparation method and carbon support on H_2O_2 electrogeneration.

2.2. Characterization of WO_3 materials

2.2.1. X-ray diffraction and X-ray photoelectron spectroscopy analysis

The tungsten-based materials were physically characterized by X-ray diffraction (XRD) using a D8 Focus diffractometer (Bruker AXS) with a $CuK\alpha$ radiation source operating in the continuous scan mode (2° min^{-1}) from 20 to 60° . The XPS analysis was conducted at a pressure of less than 10^{-6} Pa using a commercial spectrometer (UNI-SPECS UHV). The $Mg K\alpha$ line was used ($h\nu = 1253.6 \text{ eV}$) and the analyzer pass energy for the high-resolution spectra was set

to 10 eV. The inelastic background of the $W 4f$, $O 1s$ e $C 1s$ electron core-level spectra was subtracted using Shirley's method. The composition of the near surface region was determined with an accuracy of $\pm 10\%$ from the ratio of the relative peak areas, which were corrected by Scofield's sensitivity factors for the corresponding elements. The spectra were fitted using multiple Voigt profiles without placing constraints. The width at half maximum (FWHM) varied between 1.0 and 2.0 eV and the precision of the peak positions was ± 0.1 eV.

2.2.2. Electrochemical characterization

The oxygen reduction reaction was analyzed by the rotating ring-disk technique using a commercial ring-disk electrode (Pine Instruments) consisting of a central glassy carbon disk (area = 0.25 cm^2) and an Au ring (area = 0.19 cm^2) with a collection efficiency of $N = 0.37$ as support for the working electrode. A platinum wire and a Hg/HgO were used as the counter electrode and the reference electrode, respectively. A 1 mol L^{-1} $NaOH$ solution was used as the supporting electrolyte, and it was prepared from a supra-pure grade reagent purchased from Merck. All electrochemical measurements were conducted with an Autolab PGSTAT 302 N potentiostat/galvanostat and the working electrodes were constructed using the configuration proposed by Assumpção et al. [6,21]. For all of the electrochemical analyses, the electrolyte was first saturated with oxygen and oxygen flow was maintained over the electrolyte during the measurements. Measurements were performed at a fixed scan rate of 5 mV s^{-1} at room temperature. An EDI101 rotator and a CTV101 speed control unit were also used. The electrode rotation rate was varied from 100 to 3600 rpm and the experiments were controlled with General Purpose Electrochemical System (GPES) software.

2.3. H_2O_2 quantification using gas diffusion electrodes

Once the best electrocatalyst for H_2O_2 electrogeneration was identified, a GDE was configured with a diameter of 2.5 cm and used as working electrode in an electrochemical cell to determine the true quantity of H_2O_2 produced by exhaustive electrolysis at different potentials as proposed by Forti et al. [14]. As reference electrode and counter electrode the $Ag/AgCl$ (Analyser) and a Pt electrode were employed, respectively and as electrolyte a 0.1 mol L^{-1} H_2SO_4 and 0.1 mol L^{-1} K_2SO_4 solution was used. An oxygen stream at 0.2 Bar was also maintained for all experiments and the H_2O_2 was quantified by reacting $500 \mu\text{L}$ of the electrolyte containing H_2O_2 with 4 mL of a solution containing $2.4 \times 10^{-3} \text{ mol L}^{-1}$ $(NH_4)_6Mo_7O_{24}$ and 0.5 mol L^{-1} H_2SO_4 . The reaction produces a yellow product, which can be detected by UV-vis at 350 nm [28,29]. The H_2O_2 concentration was determined from a previously constructed analytical curve using a Varian Cary 50 instrument.

2.4. Phenol degradation by AOPs

Once the highest production of H_2O_2 using a GDE composed of tungsten oxide nanoparticles was determined, the best potential for H_2O_2 electrogeneration was selected for the degradation of 350 mL of 100 mg L^{-1} phenol (Sigma–Aldrich) in a solution containing 0.1 mol L^{-1} H_2SO_4 and 0.1 mol L^{-1} K_2SO_4 . For these experiments the same electrochemical cell used for the H_2O_2 production was employed at the same conditions. For phenol degradation, several methods were employed: photodegradation, electrodegradation, photo-electrodegradation, electro-Fenton and photo-electro-Fenton processes. In all photo-processes, we used an UV radiation source from a 9 W mercury lamp (Pen Ray Power Supply, model PS-1 from UVP). For the Fenton-process, we added $3 \times 10^{-3} \text{ mol L}^{-1}$ iron (II) sulfate (Fe^{2+}) to the 100 mg L^{-1} phenol solution, which was subject to degradation. All of the

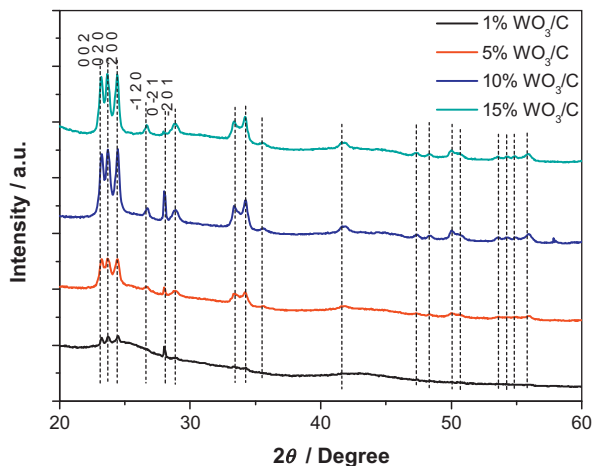


Fig. 1. XRD patterns of tungsten oxide nanoparticles at different proportions (w/w) on Vulcan XC 72R carbon.

degradation reactions were performed using the same electrochemical cell employed to quantify the H_2O_2 concentration.

The degradation reactions were monitored using high performance liquid chromatography (HPLC) and total organic carbon (TOC) analyses. For HPLC analysis, the samples were first filtered through a Millipore 0.45 mm Durapore PVDF filter (13 mm diameter) and then analyzed immediately following collection from the electrochemical cell. The phenol concentration was monitored using a Shimadzu 20A HPLC equipped with a C-18 column (250 mm \times 4.6 mm, i.d. \times 5 μm particle size) at 40 °C, a mobile phase composed of methanol: 1% acetic acid solution (30:70, v/v) and a flow rate of 1 mL min^{-1} . The injection volume and the detection wavelength were 20 μL and 280 nm (UV-Vis SPD-20A) [30]. The phenol concentration was calculated by a previously constructed analytical curve and the TOC content was analyzed by the direct injection of the samples into a Shimadzu TOC-VCPN analyzer.

The phenol degradation samples following 12 h of exhaustive electrolysis were injected on a Varian 3800 GC equipped with an ion trap Saturn 2200 mass spectrometer, using autosampler in an Agilent DB-5 column (30 m \times 0.25 mm with 0.25 μm). The injector program consisted of holding at 250 °C during the analysis and the column program consisted of holding at 70 °C for 1 min with heating from 70 °C to 170 °C at a rate of 20 °C min^{-1} , holding for 24 min and a split of 1/20. In the mass spectrometer, 50 μA energy emission was used with a reaction time of 120 μs for a mass range of 40–650 m/z .

3. Results and discussion

3.1. XRD and XPS analysis

Fig. 1 shows the XRD patterns of the WO_3/C electrocatalysts at 1%, 5%, 10% and 15% (w/w) prepared by the PPM and supported on Vulcan XC 72R. The XRD patterns demonstrate that these materials contained predominantly the WO_3 phase according to JCPDF # 32-1395. **Fig. 2** presents the XRD patterns of the 1% WO_3/C material prepared by two different methods (SGM and PPM) and supported on two different carbon sources (Vulcan XC 72R and Printex L6).

Sriyudthsak et al. [31] in their study with WO_3 powder, prepared by the precipitation technique, observed that the major crystalline planes of WO_3 were (002), (020) and (200). Our study demonstrated similar findings as shown in our XRD analysis (**Fig. 1**). Moreover, they [31] observed that increasing calcination temperature increased the degree of crystallinity. In their study, the authors used calcination temperatures between 300 °C and 800 °C, while

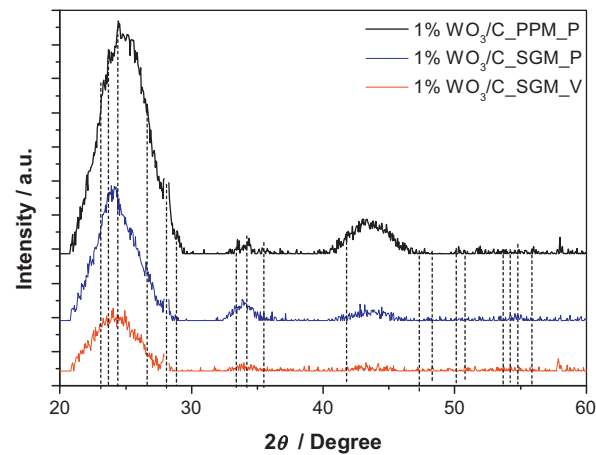


Fig. 2. XRD patterns of tungsten oxide nanoparticles using different methodologies and carbon substrates.

our study used a thermal treatment of 400 °C. This difference in the temperature may explain the low crystallinity observed in our XRD analysis (**Fig. 2**).

Fig. 3 displays the deconvoluted XPS W 4f core level spectra of tungsten oxide nanoparticles containing 1% WO_3/C supported on Vulcan XC 72R (1% WO_3/C _SGM_V) or Printex L6 (1% WO_3/C _SGM_P), both compounds prepared by the sol-gel process. The noisy signal of the samples is due to the low tungsten content (nominal 0.06 at.%), being close to the detection limit. The Printex sample contains a slightly higher concentration of tungsten (0.3 at.%) than the Vulcan-supported sample (0.2 at.%). Nevertheless, both spectra were fitted with good precision by only one spin-orbit doublet attributed the W^{6+} oxidation state, centered at a characteristic binding energy of 35.6 eV ($\text{W} 4\text{d}_{7/2}$) [32]. The fitted C 1s core level spectra, displayed in **Fig. 4**, show for both samples five different chemical environments of carbon with the predominance of disordered aliphatic C–H phase separated approximately 1.3 eV from the aromatic C–C phase located at a binding energy of 284.4 eV. The high intensity of this sub-peak is related to the presence of a large number of C–H groups formed during the sol-gel process. The carbon–oxygen groups, located at the high binding energy tail of the

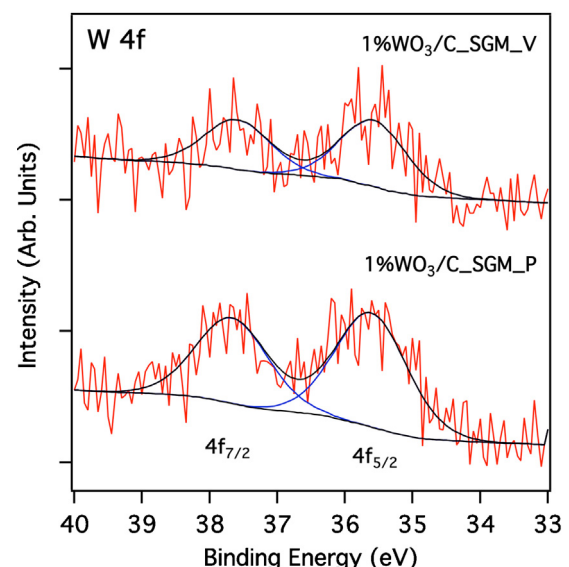


Fig. 3. Fitted XPS W 4f spectra of tungsten oxide nanoparticles containing 1% WO_3/C on Vulcan XC 72R and Printex L6 carbon support prepared by SGM.

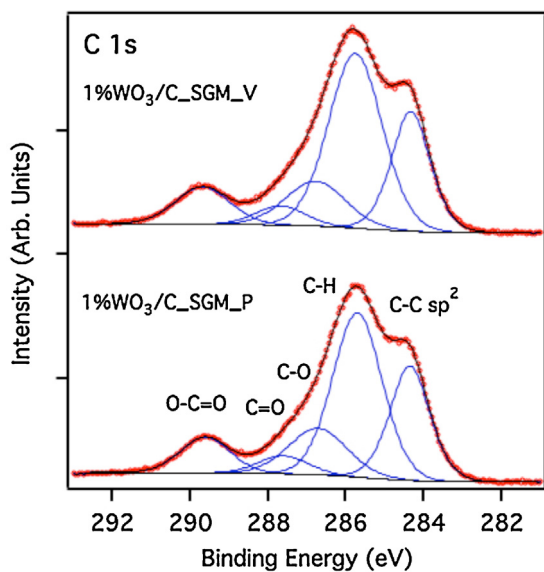


Fig. 4. Fitted XPS C 1s spectra of tungsten oxide nanoparticles containing 1% WO_3/C on Vulcan XC 72R and Printex L6 carbon support prepared by SGM.

spectrum, contain bridging C—O (286.7 eV), carbonyl (287.7 eV) and also a high concentration of carboxylic groups (289.6 eV). The latter groups constitute the main part of the surface layer and thus contribute to the elevated oxygen concentration of both samples, which is approximately 16 at.%.

3.2. Electrochemical characterization

Oxygen can be completely reduced to water with the concomitant consumption of four electrons per O_2 molecule. Or alternatively, oxygen can be partially reduced, forming H_2O_2 as an intermediate, with only two electrons exchanged per O_2 molecule [33]. To determine which pathway was followed, the tungsten electrocatalyst activity on the ORR was evaluated using a rotating ring-disk electrode technique. Fig. 5 compares the polarization curves for the oxygen reduction of 1%, 5%, 10% and 15% WO_3/C compounds prepared by PPM and supported on Vulcan XC 72R, Vulcan XC-72R carbon and Pt/C E-TEK catalysts. In Fig. 5, the polarization curves for the disk show the same general shape for all

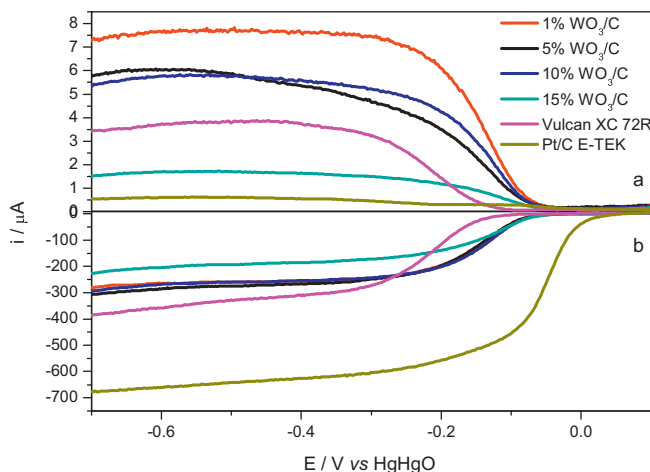


Fig. 5. Steady state polarization curves for ORR on different proportions of tungsten oxide materials on carbon, Vulcan XC-72R and Pt/C E-TEK in oxygen-saturated 1 mol L^{-1} NaOH at a scan rate of 5 mV s^{-1} . (a) Ring current $E_{\text{ring}} = 0.2 \text{ V}$. (b) Disk current at 1600 rpm.

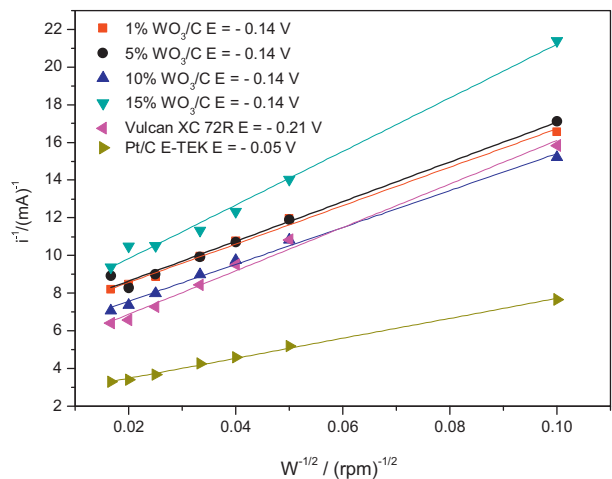


Fig. 6. Koutecky-Levich plot for ORR on different proportions of tungsten oxide materials.

tungsten materials; the curves also exhibit a disk-current that is similar to Vulcan XC 72R, indicating a 2-electron transfer in ORR [34]. Among all of the tungsten materials studied, the 1% WO_3/C material exhibited the highest ring current, which corresponds to the highest amount of H_2O_2 produced. Pt/C showed the lowest ring current, which was expected because Pt/C is a reference material for the 4-electron pathway or water production [35]. The 1% WO_3/C catalyst yielded the best average results once this material presented the highest ring current of all tungsten-modified catalysts studied. The ring-current of the 1% WO_3/C catalyst was also higher than that of carbon powder, a reference material for H_2O_2 production. Furthermore, the onset potential for the peroxide generation of all tungsten-based materials was much lower than that of Vulcan XC 72R, which is a substantial improvement in the electrocatalytic performance and may have direct implications on electric energy consumption.

The ORR data for all compositions of the tungsten materials presented in Fig. 5 were also analyzed using the Koutecky-Levich (K-L) equation [36]. Fig. 6 presents the corresponding K-L plots for all proportions of tungsten-based electrocatalysts. The slopes of these curves are directly proportional to the number of electrons exchanged in the ORR. The slopes obtained for the 1% WO_3/C and 5% WO_3/C catalysts were 102 and 105 $(\text{rpm})^{1/2} (\text{mA})^{-1}$, respectively. These slopes were very close to the value obtained for carbon, 115 $(\text{rpm})^{1/2} (\text{mA})^{-1}$, and quite different from the value obtained for Pt/C, 53 $(\text{rpm})^{1/2} (\text{mA})^{-1}$. These results suggest that the 2-electron transfer occurs for the tungsten-based materials in ORR because carbon and Pt/C are reference materials for the 2- and 4-electron oxygen reduction to hydrogen peroxide or water, respectively [35]. However, the number of electrons transferred during the ORR and the H_2O and H_2O_2 percentages was also calculated according to Demarconnay et al. [37] and Jakobs et al. [38] and it is presented at Table 1.

Considering that the preparation methodology [21] and the carbon supports [6] could also influence the hydrogen peroxide production, the 1% WO_3/C catalyst, identified as the best electrocatalyst for H_2O_2 electrogeneration, was also prepared by PPM and SGM and supported by two types of carbon, Printex L6 and Vulcan XC 72R. Fig. 7 displays the polarization curves for ORR on the 1% WO_3/C catalyst prepared by SGM and supported on Printex L6 (1% $\text{WO}_3/\text{C}_\text{SGM.P}$), on the 1% WO_3/C catalyst prepared by PPM and supported on Printex L6 (1% $\text{WO}_3/\text{C}_\text{PPM.P}$), on the 1% WO_3/C catalyst prepared by SGM and supported on Vulcan XC 72R (1% $\text{WO}_3/\text{C}_\text{SGM.V}$), on Vulcan XC 72R, on Printex L6 and on Pt/C E-TEK. In Fig. 7, the polarization curves for the disk on the tungsten

Table 1

Number of electrons transferred and H_2O and H_2O_2 percentages formed during the ORR for all tungsten based materials.

Material	n_t	$p(H_2O)$	$p(H_2O_2)$
$WO_3/C\ 1\%_{-}MPP_V$	2.3	16	84
$WO_3/C\ 5\%_{-}MPP_V$	2.4	22	78
$WO_3/C\ 10\%_{-}MPP_V$	2.4	22	78
$WO_3/C\ 15\%_{-}MPP_V$	3.2	61	39
$WO_3/C\ 1\%_{-}MSG_P$	2.4	19	81
$WO_3/C\ 1\%_{-}MPP_P$	2.5	24	76
$WO_3/C\ 1\%_{-}MSG_V$	2.3	14	86
Printex L6	2.4	22	78
Vulcan XC 72R	2.9	44	56
Pt/C E-Tek	4.0	100	0

materials show a disk-current that is similar to Vulcan XC 72R and Printex L6 and quite different from Pt/C E-Tek, indicating again a 2-electron transfer in ORR.

Among all of the tungsten materials prepared from different methodologies and different supports, the $1\%_{-}WO_3/C_SGM_V$ catalyst exhibited the highest ring current, which is a consequence of the highest amount of H_2O_2 produced. This material presented the highest ring current of all tungsten-modified catalysts studied. The ring-current of $1\%_{-}WO_3/C_SGM_V$ was also higher than that of carbon powder, a reference material for H_2O_2 production and higher than that of $1\%_{-}WO_3/C_PPM_V$, indicated as the best electrocatalyst in Fig. 5.

The ORR data obtained in Fig. 7 were also analyzed using the K-L equation. Fig. 8 shows the corresponding K-L plots for all electrocatalysts that were prepared using different methodologies and different carbon supports. The slope obtained for $1\%_{-}WO_3/C_SGM_V$ was $106\ (rpm)^{1/2}\ (mA)^{-1}$ and was very close to the value obtained for Printex L6 ($105\ (rpm)^{1/2}\ (mA)^{-1}$) and Vulcan XC 72R ($115\ (rpm)^{1/2}\ (mA)^{-1}$). Furthermore, the $1\%_{-}WO_3/C_SGM_V$ slope was not similar to that obtained for Pt/C ($53\ (rpm)^{1/2}\ (mA)^{-1}$) using the same process. Since carbon and Pt/C are reference materials for the 2 and 4-electron oxygen reduction to peroxide and water, respectively [35] the results indicate that the peroxide pathway is preferentially followed for $1\%_{-}WO_3/C_SGM_V$. These results further confirm the results presented in Fig. 7. However, the number of electrons transferred (n_t) during the ORR and the H_2O ($p(H_2O)$) and H_2O_2 ($p(H_2O_2)$) percentages was also calculated according to Demarconnay et al. [37] and Jakobs et al. [38] and it is presented at Table 1.

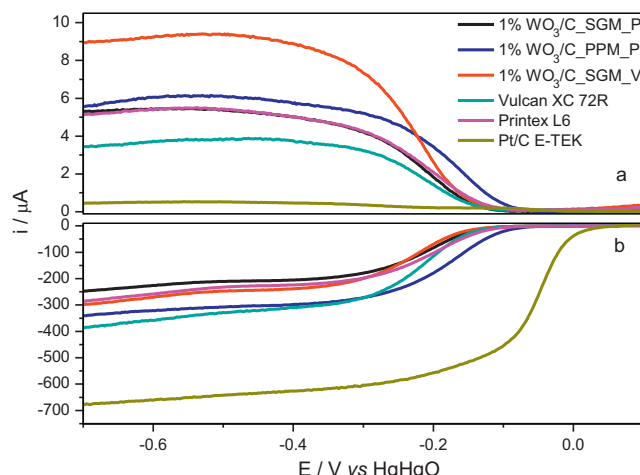


Fig. 7. Steady state polarization curves for ORR on tungsten oxide materials using different methodologies and carbon substrates in oxygen-saturated $1\ mol\ L^{-1}$ NaOH at a scan rate of $5\ mV\ s^{-1}$. (a) Ring current $E_{ring} = 0.2\ V$. (b) Disk current at $1600\ rpm$.

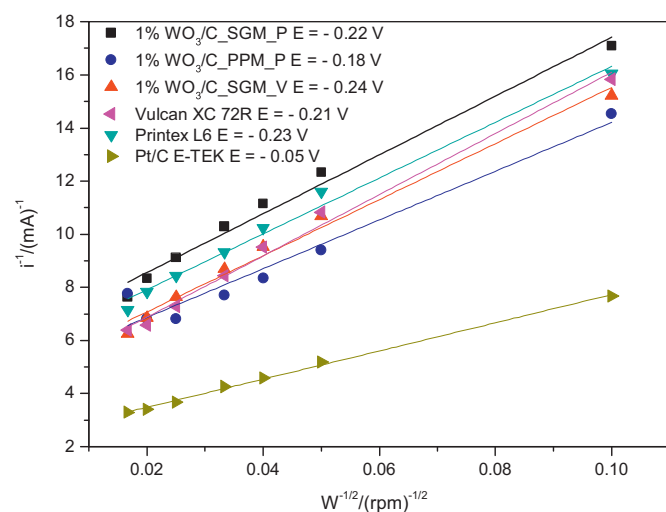


Fig. 8. Koutecky-Levich plot for ORR on tungsten oxide materials using different methodologies and carbon substrates.

Many studies related to WO_3 deposited on various supports have demonstrated that this catalyst exhibits surface acidity issued from the presence of Lewis and Brønsted acidic sites related to W^{6+} species [39] and that the acid surface has a higher affinity for species with OH^- , which could provide more hydrophilicity and consequently higher activity in the ORR for H_2O_2 production [6]. Furthermore, previous studies have demonstrated that lower quantities of metal on carbon supports are more active for hydrogen peroxide formation [22,40]. Additionally, $1\%_{-}WO_3/C_SGM_V$ presents elevated oxygen concentrations, favoring H_2O_2 production as discussed before for $4\%_{-}CeO_2/C$ nanomaterials (Assumpção et al. [22]).

3.3. H_2O_2 quantification using gas diffusion electrodes

Once the best electrocatalyst for H_2O_2 electrogeneration was identified, a GDE composed of $1\%_{-}WO_3/C_SGM_V$ was configured and used in an electrochemical cell as working electrode to determine the true quantity of H_2O_2 . For all measurements, an Ag/AgCl (Analyser) and Pt wire were used as reference and counter-electrode, respectively. Fig. 9 shows the H_2O_2 production as a function of the electrolysis time at different applied potentials in acid media. The H_2O_2 concentration was quantified using a calibration curve obtained over the concentration range of $1\text{--}1000\ mg\ L^{-1}$ with a correlation coefficient of 0.999: $Abs = -0.0695 + 0.00132C_{H_2O_2}$.

The best potential for H_2O_2 electrogeneration using the GDE composed of tungsten was $-1.3\ V$, which yielded an H_2O_2 concentration of $585\ mg\ L^{-1}$. Experiments conducted with GDE composed of Vulcan XC 72R carbon at the same conditions (electrolyte solution and applied potential) produced $100\ mg\ L^{-1}$ of H_2O_2 as observed in Fig. 9, indicating that the major production of H_2O_2 occurred using the material composed of tungsten. These results confirm that the presence of tungsten oxide nanoparticles within the GDE matrix enhances the two-electron ORR, which is most likely associated with the presence of more oxygenated acid species as shown in the XPS results and by the presence of Lewis–Brønsted acidic sites related to W^{6+} species [39]. The acidic sites have a higher affinity for species with OH^- , which may provide greater hydrophilicity and consequently higher activity in the ORR for H_2O_2 production.

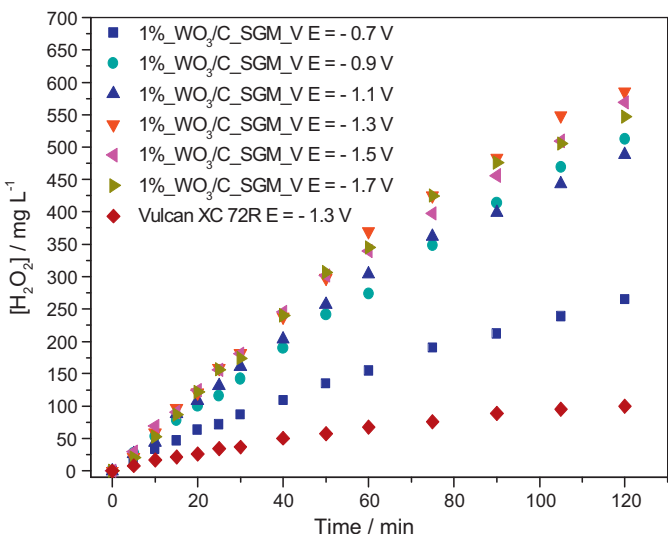


Fig. 9. H₂O₂ concentration as a function of electrolysis time at different applied potentials using 1% WO₃/C supported on Vulcan XC 72R and prepared by SGM. Vulcan XC 72R at -1.3 V inserted for comparison. Supporting electrolyte: 0.1 mol L⁻¹ K₂SO₄ and 0.1 mol L⁻¹ H₂SO₄. O₂ pressure = 0.2 bar.

3.4. Phenol degradation by AOPs

After confirming the increased production of H₂O₂ with the GDE composed of tungsten oxide nanoparticles, the best potential for H₂O₂ electrogeneration was selected for the degradation of 350 mL of 100 mg L⁻¹ phenol. The phenol concentration was determined using a calibration curve constructed over the range of 6–120 mg L⁻¹ with a correlation coefficient of 0.9999; area = 0.196 + 9.983 × 10⁻⁵ C_{phenol}.

Fig. 10 presents the phenol degradation by photodegradation, electrodegradation, photo-electrodegradation, electro-Fenton degradation and photo-electro-Fenton degradation. The experiments that involved potential application ("eletro") it was applied -1.3 V because it was the best potential for H₂O₂ electrogeneration, as observed in Fig. 9.

From the results presented in Fig. 10, it is possible to observe some degradation of phenol using only the photodegradation (UV) method, which produced degradation of nearly 10%. With the electrodegradation (H₂O₂) method was observed an

Table 2
TOC values for the phenol degradation using different AOP.

Process	Fenton_UV	Fenton	H ₂ O ₂ _UV	UV	H ₂ O ₂
Time = 0 h	74.0	75.7	74.9	73.6	73.4
Time = 2 h	66.6	71.7	69.5	73.5	70.1
Removal (%)	10.0	5.3	7.2	0.0	4.5

improvement, yielding about 35% of phenol degradation. When the electrodegradation was combined with the photodegradation (H₂O₂_UV) method, greater degradation, was observed (approximately 45%). However, the phenol degradation was substantial when the electro-Fenton process (Fenton) and the electro-Fenton associated with UV (Fenton_UV) method were employed. Using these processes, a phenol degradation of approximately 65% was obtained.

Huang et al. [41], who worked with phenol degradation in a cylindrical batch reactor (at pH = 3, phenol concentration of 200 mg L⁻¹, iron (II) concentration of 5 mg L⁻¹ and H₂O₂ concentration of 1080 mg L⁻¹), identified a phenol degradation of 50% in 120 min by the UV/H₂O₂ process. This result is similar to those obtained in this paper, where we observed a phenol degradation of 45% using nearly half of the H₂O₂ amount under the same UV/H₂O₂ conditions. Huang et al. [41] also observed an improvement in phenol degradation using the Fenton and photo-Fenton processes. Additionally, Kavitha et al. [42] studied phenol degradation by AOPs using a batch model (at pH = 3, phenol concentration of 2.12 mol L⁻¹, H₂O₂ concentration of 30 × 10⁻³ mol L⁻¹ and iron concentration of 0.8 × 10⁻³ mol L⁻¹) and observed high levels of phenol degradation (82%) using the Fenton reaction. Using our methodology and the electro-Fenton process, we observed a phenol degradation of 65% using nearly half of the amount of H₂O₂ that was used by Kavitha [42]. It is important to stress that in the Huang et al. [41] and Kavitha et al. [42] studies, the H₂O₂ was added into the solution and not electrogenerated as in this work.

The efficient degradation of phenol using electro-Fenton processes can be explained by the fact that Fe (II) ions react with H₂O₂ to produce the hydroxyl radical that attacks the π system of the aromatic phenolic ring in a rapid manner, resulting in an efficient degradation [41,42].

The TOC data for the phenol degradation using different AOPs are presented in Table 2. From these results, it is possible to confirm that mineralization does not occur during the photodegradation (UV) of phenol. There is mineralization of approximately 5% using the electrodegradation (H₂O₂), electrodegradation associated with UV (H₂O₂_UV) and electro-Fenton process (Fenton). For the electro-Fenton associated with UV (Fenton_UV) method, mineralization of approximately 10% is observed; thus, the electro-Fenton associated with UV process is most suited for phenol degradation.

Because only minimal mineralization was observed over the course of 120 min (10% phenol mineralization in Fenton_UV), we performed an exhaustive electrolysis for the duration of 12 h. From this experiment, we observed no phenol after 4 h of reaction time, indicating that all phenol was degraded by this time point. The TOC data for the phenol degradation over the course of 12 h are presented in Table 3.

Table 3 demonstrates that the phenol mineralization was 75.4% after 12 h of exhaustive electrolysis. During the phenol degradation, it was possible to observe a color modification from colorless to brown and this color was then changed to light yellow and finally clear. This color change was also observed by other authors [41,42]. The brown color was eliminated as the reaction proceeded during the 12 h experiment, indicating phenol mineralization as observed by the TOC analysis. During the 12 h exhaustive electrolysis of phenol, the samples were analyzed each hour in a GC-Ms/Ms with the

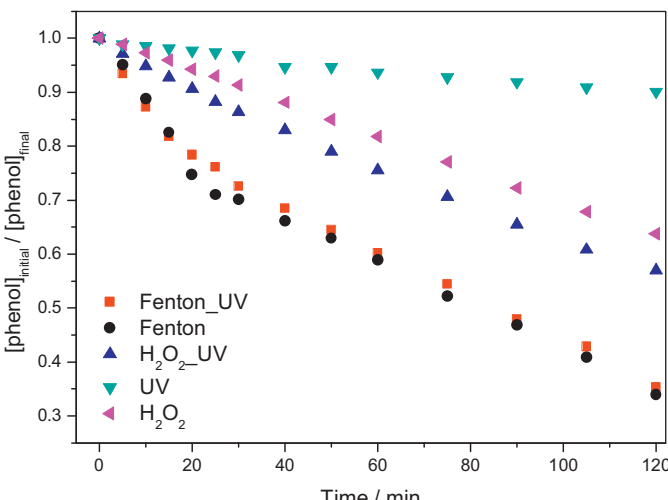


Fig. 10. Phenol concentration as a function of time at different AOP using a GDE composed of tungsten in 0.1 mol L⁻¹ K₂SO₄ and 0.1 mol L⁻¹ H₂SO₄.

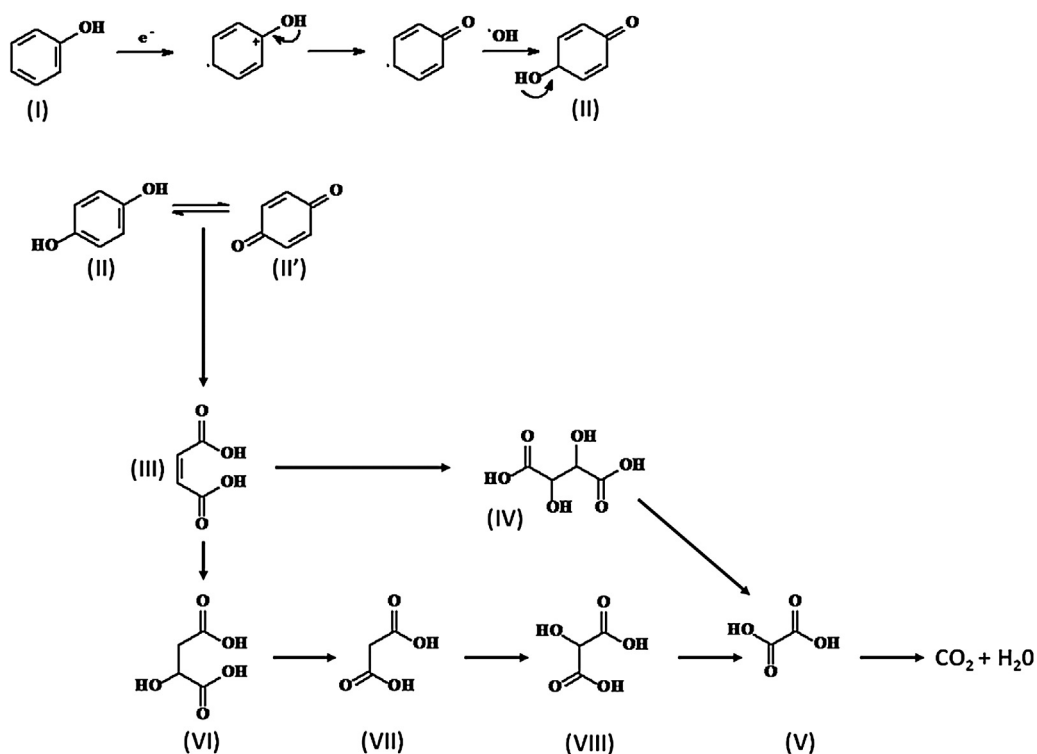


Fig. 11. Summarized pathway for the degradation of phenol during 12 h exhaustive electrolyze.

objective of determining at which step the degradation products were formed in the process of mineralization, as shown in Fig. 11.

As shown in Fig. 11, the phenol (I) has an OH group in its structure, which activates the *ortho* and *para* positions in the aromatic ring; the *para* position is preferred. Thus, in a medium that contains hydroxyl radical (H_2O_2 in the presence of Fe^{2+}), hydroquinone (II) is formed and converts to the benzoquinone (II') tautomer.

In this step, hydroxylation occurs in the double bond, with consequent rupture of the aromatic ring; thus, aliphatic compounds can now be identified. Maleic acid (III), containing a double bond, is the principal intermediate formed. This intermediate may be doubly hydroxylated to form tartaric acid (IV). Tartaric acid undergoes successive hydroxylation and decarboxylation processes to generate oxalic acid (V). Maleic acid (III) can also undergo hydroxylation of its double bond in one position to form malic acid (VI). Malic acid is subjected to successive hydroxylation and decarboxylation processes, which generates malonic acid (VII).

Malonic acid (VII) has a C_α that is highly activated due to its position adjacent to the carboxyl group. The C_α is susceptible to attack by the hydroxyl radical, generating 3-hydroxypropanedioic acid (VIII); this intermediate undergoes successive rounds of decarboxylation and hydroxylation to form oxalic acid (V). Finally, oxalic acid can undergo breaking of the carbon–carbon bond to form CO_2 and H_2O . The formation of the degradation products is compatible

with the values of TOC removal. The formation of oxalic acid, the last degradation product, was detected before the formation of CO_2 .

4. Conclusions

Among the tungsten electrocatalysts studied, the 1% WO_3/C catalyst was the most promising with respect to H_2O_2 production. However, when the preparation method and the carbon support were also taken into account, the 1% WO_3/C catalyst supported on Vulcan XC 72R and prepared by the SGM was the most efficient for H_2O_2 production. This material was analyzed using a GDE, producing 585 mg L^{-1} of H_2O_2 in acid medium; this H_2O_2 production is five times higher than the value obtained using the Vulcan carbon reference material.

The increase in H_2O_2 production by the addition of a small amount of tungsten can be explained by the fact that this material exhibits surface acidity due to the presence of Lewis–Brønsted acidic sites related to W^{6+} species. Additionally, the acid surface has a higher affinity for species with OH^- , which provides more hydrophilicity and consequently higher activity in the ORR for H_2O_2 production. These results are associated with the higher content of oxygenated acid species, which are identified by the XPS analysis. Furthermore, other studies have demonstrated that lower quantities of metal on carbon supports are more efficient for hydrogen peroxide formation.

With respect to phenol degradation, the photo-electro-Fenton method was the most efficient, as it degrades approximately 65% and mineralizes approximately 10% of the phenol in 120 min. In the 12 h exhaustive electrolysis total phenol degradation was observed in 4 h, and the mineralization was maximized (~75%) after 12 h. Substantial degradation was observed with the photo-electro-Fenton method, which was expected because the UV and Fenton processes increase the hydroxyl radical content and hydroxyl radicals are more oxidizing than H_2O_2 . In the exhaustive electrolysis experiment, we identified expected intermediate products during phenol degradation by the hydroxyl radical; these products

Table 3
TOC values for the phenol degradation during 12 h exhaustive electrolysis (Fenton–UV).

Time (h)	TOC (ppm)	Removal (%)
0	73.3	0.0
2	66.6	9.1
4	60.0	18.2
6	47.4	35.3
8	34.2	53.3
10	23.4	68.1
12	18.0	75.4

included maleic acid, tartaric acid, malonic acid and oxalic acid, giving the pathway for the degradation of phenol until the formation of CO₂.

Acknowledgments

The authors wish to thank the Brazilian Funding Institutions, CNPq (577292/2008-0, 473308/2010-0, 470172/2010-0, 150639/2013-9), CAPES and FAPESP (2005/59992-6, 2008/58789-0, 2009/09145-6, 2010/04539-3, 2010/16511-6, 2007/04759-0, 2011/14314-1, 2012/03516-5) and UFABC for their financial support. Additionally, we would like to thank the Instituto Nacional de Ciência e Tecnologia (INCT) de Energia e Meio Ambiente (Process Number 573.783/2008-0).

References

- [1] X.-Y. Li, H.P. Chu, *Water Research* 37 (2003) 4781–4791.
- [2] J.C. Bourgeois, M.E. Walsh, G.A. Gagnon, *Water Research* 38 (2004) 1173–1182.
- [3] Y.-Q. Wang, B. Gu, W.-L. Xu, *Journal of Hazardous Materials* 162 (2009) 1159–1164.
- [4] M. Li, C. Feng, W. Hu, Z. Zhang, N. Sugiura, *Journal of Hazardous Materials* 162 (2009) 455–462.
- [5] J. Zhou, X. Yu, C. Ding, Z. Wang, Q. Zhou, H. Pao, W. Cai, *Journal of Environmental Sciences* 23 (2011) 22–30.
- [6] M.H.M.T. Assumpção, R.F.B. De Souza, D.C. Rascio, J.C.M. Silva, M.L. Calegaro, I. Gaubeur, T.R.L.C. Paixão, P. Hammer, M.R.V. Lanza, M.C. Santos, *Carbon* 49 (2011) 2842–2851.
- [7] I. Gültekin, N.H. Ince, *Journal of Environmental Management* 85 (2007) 816–832.
- [8] E.R.L. Tiburtius, P. Peralta-Zamora, A. Emmel, *Journal of Hazardous Materials* 126 (2005) 86–90.
- [9] M.S. Yalfani, S. Contreras, F. Medina, J. Sueiras, *Applied Catalysis B: Environmental* 89 (2009) 519–526.
- [10] A. Nezamzadeh-Ejhieh, Z. Salimi, *Applied Catalysis A: General* 390 (2010) 110–118.
- [11] C. Lee, J. Yoon, U. Von Gunten, *Water Research* 41 (2007) 581–590.
- [12] B. Gozmen, B. Kayan, A.M. Gizar, A. Hesenov, *Journal of Hazardous Materials* 168 (2009) 129–136.
- [13] M. Giomo, A. Buso, P. Pier, G. Sandonà, B. Boye, G. Farnia, *Electrochimica Acta* 54 (2008) 808–815.
- [14] J.C. Forti, R.S. Rocha, M.R.V. Lanza, R. Bertazzoli, *Journal of Electroanalytical Chemistry* 601 (2007) 63–67.
- [15] D. Fatta-Kassinos, M.I. Vasquez, K. Kümmerer, *Chemosphere* 85 (2011) 693–709.
- [16] A.J. Poole, *Water Research* 38 (2004) 3458–3464.
- [17] Z.M. Qiang, J.H. Chang, C.P. Huang, *Water Research* 36 (2002) 85–94.
- [18] K.S. Yang, G. Mul, J.A. Moulijn, *Electrochimica Acta* 52 (2007) 6304–6309.
- [19] E. Lobnytseva, T. Kallio, N. Alexeyeva, K. Tammeveski, K. Kontturi, *Electrochimica Acta* 52 (2007) 7262–7269.
- [20] F.Y. Xu, T.S. Song, Y. Xu, Y.W. Chen, S.M. Zhu, S.B. Shen, *Journal of Rare Earths* 27 (2009) 128–133.
- [21] M.H.M.T. Assumpção, D.C. Rascio, J.P.B. Ladeia, R.F.B. De Souza, E.T. Neto, M.L. Calegaro, R.T.S. Oliveira, I. Gaubeur, M.R.V. Lanza, M.C. Santos, *International Journal of Electrochemical Science* 6 (2011) 1586–1596.
- [22] M.H.M.T. Assumpção, A. Moraes, R.F.B. De Souza, I. Gaubeur, R.T.S. Oliveira, V.S. Antonin, G.R.P. Malpass, R.S. Rocha, M.L. Calegaro, M.R.V. Lanza, M.C. Santos, *Applied Catalysis A: General* 411 (412) (2012) 1–6.
- [23] X. Chang, S. Sun, J. Han, *Materials Letters* 65 (2011) 552–554.
- [24] M. Deepa, P. Singh, S.N. Sharma, S.A. Agnihotry, *Solar Energy Materials and Solar Cells* 90 (2006) 2665–2682.
- [25] H. Habazaki, Y. Hayashi, H. Konno, *Electrochimica Acta* 47 (2002) 4181–4188.
- [26] D. Deniz, D.J. Frankel, R.J. Lad, *Thin Solid Films* 518 (2010) 4095–4099.
- [27] H.B. Suffredini, V. Tricoli, L.A. Avaca, N. Vatistas, *Electrochemistry Communications* 6 (2004) 1025–1028.
- [28] X.S. Chai, Q.X. Hou, Q. Luo, J.Y. Zhu, *Analytica Chimica Acta* 507 (2004) 281–284.
- [29] J.C. Forti, J.A. Nunes, M.R.V. Lanza, R. Bertazzoli, *Journal of Applied Electrochemistry* 37 (2007) 527–532.
- [30] Z. Guo, R. Ma, G. Li, *Chemical Engineering Journal* 119 (2006) 55–59.
- [31] M. Sriyudthasak, S. Supothina, *Sensors and Actuators B: Chemical* 113 (2006) 265–271.
- [32] NIST X-ray Photoelectron Spectroscopy Database, AV., Naumkin, A., Kraut-Vass, S.W., Gaarenstroom, C.J., Powell, NIST Standard Reference Database 20 v. 4.1, <http://srdata.nist.gov/XPS/>
- [33] P. Hernandez-Fernandez, S. Rojas, P. Ocon, J.L.G. de la Fuente, P. Terreros, M.A. Pena, J.L. Garcia-Fierro, *Applied Catalysis B: Environmental* 77 (2007) 19–28.
- [34] A. Alvarez-Gallegos, D. Pletcher, *Electrochimica Acta* 44 (1998) 853–861.
- [35] J. Vazquez-Arenas, D. Higgins, Z. Chen, M. Fowler, Z. Chen, *Journal of Power Sources* 205 (2012) 215–221.
- [36] S. Svetlana, *Electrochimica Acta* 56 (2011) 1597–1604.
- [37] L. Demarconnay, C. Coutanceau, J.M. Léger, *Electrochimica Acta* 49 (2004) 4513–4521.
- [38] R.C.M. Jakobs, L.J.J. Janssen, E. Barendrecht, *Electrochimica Acta* 30 (1985) 1085–1091.
- [39] V. Keller, P. Bernhardt, F. Garin, *Journal of Catalysis* 215 (2003) 129–138.
- [40] F. Xu, T. Song, Y. Xu, Y. Chen, S. Zhu, S. Shen, *Journal of Rare Earths* 27 (2009) 128–133.
- [41] Y.-H. Huang, Y.-J. Huang, H.-C. Tsai, H.-T. Chen, *Journal of the Taiwan Institute of Chemical Engineers* 41 (2010) 699–704.
- [42] V. Kavitha, K. Palanivelu, *Chemosphere* 55 (2004) 1235–1243.